Increased Occurrence and Intensity of Consecutive Rainfall Events in the China's Three Gorges Reservoir Area under Global Warming

Yanxin Zheng[1], Shuanglin Li[2,3], and Kalim Ullah[4]

1. Department of Atmospheric Science, China University of Geosciences, Wuhan 430074
2. Institute of Atmospheric Physics and Climate Change Research Center, Chinese Academy of Sciences, Beijing 100029
3. College of Earth and Planetary Sciences, University of Chinese Academy of Sciences, Beijing 100049
4. Department of Meteorology, COMSATS Institute of Information Technology (CIIT), Islamabad, Pakistan

To be submitted to earth and space science.

Corresponding author email: *shuanglin.li@mail.iap.ac.cn*

Abstract

Consecutive Rainfall Events (CREs) are important triggers of geological hazards like landslide downhill and mudslide in the Three Gorges Reservoir area (TGR), China. These hazards are not only potential risks for the effective storage capacity of the reservoir but also threats of the safety of the reservoir's Great Dam. The future changes of CREs' occurrence and intensity are analyzed by using the projection experiments from twenty models attending the Coupled Model Inter-comparison Project phase 5 (CMIP5) under three different representative concentration pathways (RCP2.6, RCP4.5 and RCP8.5). Spring and fall are focused on, during which CREs are most frequent. Considering a common overestimate of rainy days number in the state-of-the-art models, a new approach is developed to define CREs based on the percentile of rainfall distribution in observations. The approach yields a similar CREs climatology in models to that in observations, and thus is used to identify CREs in models. The results based on multiple model ensemble (MME) and model spread comparison suggest a significant increase in spring and an overall decrease in fall in CREs' occurrence under all three scenarios. As for the intensity, it is projected to intensify both in spring and fall. Particularly, the higher the emission scenario, the greater the spring accumulated rainfall amount during a single CRE. These results imply an increasing risk of geological hazards in the TGR in the future.

1. Introduction

The Three Gorges Reservoir area (TGR), spanning 28-32°N latitudinally and 105-112°E longitudinally (see Figure 1), is a mountainous, highly populated region locating in the middle reach of the Yangtze River basin, central China. It often suffers from geological disasters like landslide and mudslide (Chen et al., 2012; Ma et al., 2006). These disasters result in tremendous damages to the lives and properties. One example is the landslide occurring in 1998, which caused a direct economic loss of 610 million RMB (Ma et al., 2005). In addition, they cause rockfall, mud and debris flows, which block the rivers running to the reservoir, reduce the effective storage of the reservoir (Zhang et al., 2016), even threaten the safety of the reservoir's Great Dam. Therefore, predicting, warning and preventing geological hazards are an important national demand in China.

Synoptic processes, especially Consecutive Rainfall Events (CREs), during which it rains for one week and even longer with a gentle and moderate intensity, are a substantial trigger to geological hazards, although other factors like short-duration heavy rainfall or earthquake can be also important (Guzzetti et al., 2007; Ye et al., 2009). Corominas and Moya (1999) illustrated that the risk of landslide increases substantially when it rains persistently for several weeks with the moderate accumulated rainfall amount over 200 mm. The size of the landslide may be positively proportional to the duration of CREs (Jibson, 2006). One recent case is the severe landslide occurring in Lishui (28.6°N, 119.9°E), Zhejiang Province on 13 November 2015, which resulted in 38 deaths (Liu, 2015). Prior to the landslide, it

74 rained lightly or moderately for nearly one month, with an intensity of only 6-8 mm
75 per day. No precursor was found and no warning was issued before the disaster. In
76 addition to trigger geological disasters, CREs adversely influence agricultural
77 production, cause local pooling or freezing rain during chilling weather, and affect
78 human health (Ding et al., 2008; Li et al., 1977; Sun et al., 2016). Therefore,
79 understanding the future trend of CREs is of substantial importance.

80 Previous analyses based on instrumental records suggest a decreasing trend in
81 spring CREs' occurrence, duration and accumulated rainfall amount, but an increase
82 in the mean daily rainfall during the past decades (Zheng et al., 2018; Zou, 2005). In
83 fall the trend is somewhat similar, with a decrease in occurrence despite an increase in
84 intensity (Sun et al., 2016; Wang and Zou, 2015). Whether such a trend persists into
85 the future is unclear.

86 Under the context of global warming, rainfall features change including its
87 occurrence frequency, duration, and intensity (Scoccimarro and Gualdi, 2013;
88 Trenberth, 1998; Zhai, 1999). Of particular importance is that rainfall becomes
89 regionalized and intensified, as far as one individual rainy event is concerned (Giorgi
90 et al., 2001; Lau et al., 2013; Sun et al., 2006). This inevitably leads to changes of
91 CREs. Thus, projecting the future trend of CREs in TGR consists of the preliminary
92 aim of the present study.

93 The reminder of this paper is organized as follows. Section 2 describes data and
94 methods. The projection experiments from the models attending the Coupled Model
95 Inter-comparison Project phase 5 (CMIP5) under three different representative

concentration pathways (RCP2.6, RCP 4.5 and RCP8.5) are used (Li et al., 2016; Sillmann et al., 2013). Because of one common bias with too many rainy days in the state-of-the-art models, the canonical method used to identify observational CREs appears inappropriate for modeled precipitation. Thus a new approach is developed for the models. Section 3 compares the CREs in the historical experiments with those in observations. Since not all models reproduce the observed CREs well, just those "good" models are selected to project the future trend. Section 4 gives the projection results based on the multiple-model ensemble mean (MME) and an assessment of result diversity in the individual models under different emission scenarios, with the focus on the accumulated rainfall amount and daily rainfall intensity in CREs. Finally, a summary and discussions are given in section 5.

2. Datasets and methods

2.1 *Datasets*

Gridded daily precipitation outputs from twenty models participating in CMIP5 are employed (Table 1). In order to treat all the models equally, only their first run (r1i1p1) is analyzed. The experiments include the historical run with historically evolving forcing for 1961-2005 and the projection runs with prescribed forcing of RCP2.6, RCP4.5 and RCP8.5 for 2006-2099 (Taylor et al., 2012). RCP2.6 is a low, peak-and-decay scenario in which radiative forcing reaches the maximum near the middle of the 21st century before decreasing to an eventual nominal level of 2.6 W/m^2. RCP4.5 is a medium stabilization scenario that follows a rising radiative forcing

pathway leading to 4.5 W/m^2 in 2100, while RCP8.5 is a high, business-as-usual emissions scenario with radiative forcing increase to 8.5 W/m^2 by 2100. Details on the CMIP5 models and their configurations are described at http://www-pcmdi.llnl.gov/.

To assess the CMIP5 models' ability in reproducing the observed CREs, the daily gauged grid precipitation dataset, referred to as CN05.1, is employed. CN05.1 was produced by data from high-resolution stations across China during the period from 1961 to 2015. It uses thin-plate smoothing splines interpolation for climatology and angular distance weighting interpolation for daily deviation before merging into the full 0.25° × 0.25° grids (Xu et al., 2009; Wu and Gao, 2013). This methodology follows the method by which the CRU dataset was created (New et al. 2000). More details about validation information of CN05.1 are given in Wu and Gao (2013). It has been used by a lot of previous studies (e.g. Chen et al., 2014; Li et al., 2020; Pan et al., 2020; Sui et al., 2015). In view of the possible mismatch in horizontal resolutions, both the simulated precipitation and CN05.1 are re-gridded to a 1.0° × 1.0° grid by using a bilinear interpolation algorithm.

2.2 *Methods*

a) Definition of CREs

In observational studies (e.g. Li, et al., 1977; Zou, 2005), one CRE is isolated when there are five or more consecutive rainy days. One rainy day is defined when the accumulated amount is greater than or equal to 0.1 mm within 24 hours from

140 00UTC to the next 00UTC. For CN05.1, because of the rain intensity diffusion and
141 extended rainy days caused by interpolation, one elevated threshold, 1 mm per day, is
142 used to define rainy days. One similar threshold was used in previous studies (Giorgi
143 et al., 2011; Mohan and Rajeevan, 2017; Salinger and Griffiths, 2001). Here one CRE
144 is defined to begin if any one of the following four cases: (1) it has at least 5
145 consecutive rainy days; (2) it has 6 or 7 rainy days within 7 or 8 consecutive days,
146 despite no 5 consecutive rainy days; (3) it has 7 or 8 rainy days within 9 to 10
147 consecutive days but has at least one rainy day within any two consecutive days,
148 although it does not meet (1) or (2) above; (4) it has more than 9 rainy days but has at
149 least one rainy day within any two consecutive days, although it does not meet (1) (2)
150 and (3) above (Sun et al., 2016; Zheng et al., 2018). The CRE termination is defined if
151 there are two consecutive non-rainy days following CRE, and the duration is the day
152 number from the beginning date until the ending date.

153 For the model outputs, the above definition is inappropriate because models
154 generally overestimate rainy day number but underestimate precipitation intensity
155 (Dai and Trenberth, 2004; Sun et al., 2007). It will cause much-more-than-observed
156 CREs if a same 1 mm threshold is used. Previous studies developed various
157 calibration methods to correct the bias. The first one is the simplest unbiasing method
158 which simply overlaps the models' climatological mean bias into the simulations
159 (Déqué, 2007). It is straightforward, but has an implicit, unrealistic assumption that
160 the modeled mean rainfall follows the observed regardless of the variance. The second
161 is a combination of local intensity scaling with power transformation. It scales the

modeled precipitation within the observations, and corrects both the climatological mean and variance (Fang et al., 2015; Schmidli et al., 2006; Teutschbein and Seibert, 2012). In details, modeled raw precipitation is calibrated by multiplying the ratio of the observed mean precipitation to the modeled. The method will cause unmatched successive days and weakened rainfall extremes. The third one is probability quantile mapping (Semenov et al., 2010; Themeßl et al., 2012). It adjusts the climatological mean, variance, and probability quantiles distribution of modeled precipitation and has no influences on the extremes of the modeled rainfall. But it fails to correct the temporal autocorrelation properties intrinsic to series, and neglects the physical connection between variables (Boé et al., 2007). The fourth is the Artificial Neural Networks (ANNs) technique. It efficiently handles the noisy and unstable data that are typical in weather station observation, and maps highly nonlinear relationships between a set of inputs and the corresponding outputs (Luk et al., 2000). The rainfall estimates from ANNs are even more accurate than those based on statistical or dynamic downscaling approaches (Mendes and Marengo, 2010; Skamarock et al., 2008). But this technique is highly sensitive to the quantity and distance of neighbouring gauges, and to the local hydrologic system as well (Hung et al., 2009).

In the present study, the long-term trend and future projection of CREs is focused on, so the rainfall intensity in a single day is relatively less important than whether it rains or not on that day. Since rainy day number may be subjective to change in all the above calibration methods, we develop a new approach to defining CREs instead. It is based on the Cumulative probability Distribution Function (CDF)

of daily rainy amount. The CDF in models is assumed to follow the observed, which is calculated based on the threshold of 1.0 mm per day. Thus for the models the threshold to define rainy days can be derived. Subsequently, rainy days number and the CREs can be easily calculated at each grid points.

b) Variable to quantify CREs

A total of four variables are used to quantify the CREs, including occurrence frequency (OCF), total rainy days (TRD), accumulated rainfall amount (ACR) and mean daily rainfall intensity (INT). The first, OCF, describes the occurrence climatology of CREs, while the latter three describe the duration and strength of one single CRE. INT is not independent of ACR and TRD, but equal to ACR divided by TRD. Previous studies suggest that all the four variables are linked to geological hazards (Corominas and Moya, 1999; Jibson, 2006), thus they are used for the present analysis. Since CREs occur most frequently in spring and fall in TGR, just these two seasons are focused on. Spring is referred to as 25 February to 4 June, while fall is referred to as 28 August to 4 December considering the possibility that CRE occurrence is not contained strictly in a whole calendar season.

c) Sen's slope estimate

Due to non-normal characteristics of probability distributions, trends of daily precipitation amount and subsequently CREs cannot be estimated by the least squared fitting. As Santos and Fragoso (2013) and Mohan and Rajeevan (2017), here the

trends are estimated by the Kendall's tau-based slop estimator (Sen's slope Q; Sen, 1968) as follows

$$Q = median\left(\frac{X_i - X_j}{t_i - t_j}\right) \quad (1).$$

Specially, for one time series with the length of L, at one time point (say t_i, i=2,…, L), slope can be calculated by using values (X_i) and (X_j) at time points t_i and t_j , respectively. Here t_j precedes t_i by at least one unit (j=1,…, i-1). As such, a total number of (L-1)! slopes can be obtained, and the median among all the slopes is the best estimate of the trend. According to Yue et al. (2002), the Sen's slope is better than the least squared fitting when estimating precipitation trend. Then, we use the least squared fitting to estimate the intercept of the trend-dominated series (Wang and Swail, 2001). Non-parametric Mann-Kendall test is used for significance validation, since it is reliable for both monotonic linear and nonlinear trends in non-normal distributed series (Gotway, 1992).

d) Metrics for model performance and selection

To assess model's ability in reproducing spatial pattern of CREs, the Taylor Diagram (Taylor, 2001) is employed, which provides a statistical comparison of simulated and observed CREs, in terms of spatial correlation coefficient, root-mean-square (RMS) difference, and standard deviation. The RMS difference and the standard deviation of various indices in the models are normalized by the observed. Thus a perfect model has the RMS difference equal to 0, and the spatial correlation and the ratio of spatial standard deviations both close to 1.

Because of no initialization for the oceanic model component in these CMIP5, one should not expect that their historical runs have the ability to reproduce the observed CREs evolution. Thus we compromise to assess their normalized temporal standard deviation δ_m/δ_o (Han et al., 2014; Santer et al., 2009). Here δ_m and δ_o denote the inter-annual standard deviation of model simulated and observed seasonal mean CREs variables, respectively. The closer to 1 the value, the better the agreement between simulation and observation is.

Considering the substantial importance of CRE occurrences, just OCF and TRD are used to select "good" models. Three criterions are used based on Taylor diagram: (1) the spatial correlation coefficient of models' CRE occurrences with the observed is above 0.31 (significant at the 95% level), (2) the normalized spatial RMS of CREs' occurrences is less than 1.5, and (3) the normalized deviation of modeled spatial CREs' occurrences is smaller than 1.5 but great than 0.5. Besides, another more criterion is considered: the normalized temporal standard deviation of simulated occurrences is smaller than 1.5 but great than 0.5.

3. Models' simulation on CREs in the historical experiments

The threshold for rainy days is derived before we evaluate the ability of the models in reproducing the observed OCF and TRD. Figure 2 compares the CDFs from the observations and the models. From it, the percentile with the cumulative probability in the observed rainy days below the threshold (1.0 mm per day) is 60.49% in spring (64.17% in fall) in all grid points. Correspondent to the same percentile, the

threshold is different from model to model. For example, for MRI-CGCM3 and CSIRO-Mk3.6.0, the threshold is 2.1 mm per day in spring, 1.0 and 0.5 mm per day in fall, respectively. The closer to 1.0 mm the derived threshold, the better the model is in capturing the observed rainy days. A higher or lower threshold indicates an overestimate or underestimate in modeled rainy days. Column 3 in table 2 gives the derived threshold for the individual models.

After the threshold is derived, simulated CREs can be calculated subsequently. Figure 3 is the Taylor diagram which compares the simulated and observed spatial distribution of CREs. About one half of the models fail to reproduce the spatial pattern of spring CREs, with the correlation less than 0.31. For fall, only a quarter of the models exhibit a significant skill. MME of all twenty models (refer to as MME_A; the character "A" means "all", refer to Table 2 and Figure 3) shows a pronounced bias. In spring, the spatial correlation coefficient in observed and MME_A OCF (TRD) is 0.74 (0.72), and the standard deviations in MME_A is underestimated relative to the observed. In fall the modeled standardized deviations are close to the observed, but the correlation coefficient is 0.38 (0.33) for the observed and model MME_A OCF (TRD), even lower than that in spring.

By applying the criterions in section 2.2d, for spring a total of 11 models (FGOALS-g2, IPSL-CM5A-LR, IPSL-CM5A-MR, CNRM-CM5, CanESM2, HadGEM2-AO, HadGEM2-ES, MIROC5, MPI-ESM-LR, MRI-CGCM3, CSIRO-Mk3.6.0) outstand as "good" models. For fall, a total of 5 models (IPSL-CM5A-LR, IPSL-CM5A-MR, CNRM-CM5, MRI-CGCM3, CSIRO-Mk3.6.0)

are selected. MME of these “good” models (refer to as MME_G; the character “G” mean “good” in Table 2 and Figure 3) exhibits an evident improvement in reproducing the observed CREs, with the spatial correlation coefficient in the observed and simulated OCF and TRD above 0.84 in spring (0.75 in fall) from these “good” models. Also, the standardized deviations in these “good” models are closer to the observed. Hereafter just the results from these “good” models are analyzed, and for brevity MME is used to represent MME_G unless it is clarified specially.

Table 2 compares the performances of these “good” models along with their MME and the observations. The seasonal mean accumulated rainfall amount (column 4) in observations in spring and fall is 328.1 and 250.3 mm, respectively, while this value in models varies from 274 to 463 mm in spring (from 163 to 256 mm in fall). The overall consistence in the models’ and the observed CREs climatology indicates a qualitative reasonability of this derived threshold. The climatological OCF in individual models and in MME is close to the observation (column 5) in both spring and fall. As for trend, in spring, the OCF in observation (column 6) exhibits a reduction, albeit a lack of significance. About a half of the models yield a same negative trend as the observed, but no significant trend is seen in the models else. The spring trend in MME is nearly neutral (0.01 times per decade), in contrast with a reduction in observations (-0.10 times per decade). In fall the trend in models bears an overall similarity to the observed, which is consistently negative among all the five “good” models albeit being less significant. Also, their MME shows a significant reduction, which is consistent with observations.

For TRD (column 7 and 8), the observed climatology is 18.1 and 18.6 days in spring and fall, respectively. This value in most of the models is slightly greater both in spring (from 18.4 to 20.5 days, except for MIROC in which it is 17.7 days) and fall (from 21 to 25.2 days). As for trend, seven models among the eleven “good” for spring and all the five “good” models for fall yield a reduction consistent with the observed (column 8). Not surprisingly, MME yields a reduction both in spring and fall, in agreement with a major of the models.

Above the models’ occurrence of CREs climatology and trends have been analyzed. The interannual variability of CREs in these models is also compared with the observations. Figure 4 (left panels to the black dashed vertical line) displays the modeled and observed OCF and TRD evolutions. From it, the uncertainty (model spread) within the models generally conforms to the observed, although the variability is less evident. These analyses suggest that the occurrence of CREs in models is overall comparable to the observed.

Based on OCF and TRD, the intensity of CREs (ACR and INT) is further investigated. The observed ACR (column 9 and 10) is 143.1 and 148.6 mm in spring and fall, respectively. The modeled value in spring is greater in most of models except for IPSL (122.3 and 125.3 mm, respectively). Six models simulate a reduction trend, consistent with the observation (-11.82 mm per 10 year). However, MME suggests an increase trend. It may be not realistic, because it is dominated by CanESM2. In fall it is less unanimous, with two models with a higher value and the three else with a lower value. All five models and their MME show a reduction trend, consistent with

observation.

The observed INT (column 11) is 7.8 and 7.9 mm per day in spring and fall, respectively. The value in spring in most of models (8.0 to 12.2 mm per day, except for two IPSL models) is slightly greater, but somewhat smaller in fall (4.8 to 7.0 mm per day). The observed INT trend exhibits negative in both the seasons. Only a small fraction of models in spring (three out of eleven models) reproduces the observed trend, but so do a major of models in fall (three out of five models) (column 12). Figure 7 (left half to the vertical black dashed line) displays the modeled ACR and INT evolutions in historical runs along with the observations. Although a comparison of the evolutions itself does not yield much meaning due to no initialization as mentioned in the above section, it can still provide insights into the interannual variability. From it, the simulated inter-model spread conforms to the observed. These analyses suggest an overall consistence of CREs in these selected models with the observed. This lays a basis for projecting CREs' future change by using these "good" models.

4. Future projections of CREs

4.1 *Occurrence*

Figure 4 (right to the black vertical dashed line) shows the projected occurrence of CREs (OCF and TRD) averaged over TGR under three emission scenarios. In spring (Figs. 4a and 4b), MME shows a significant increase in OCF and TRD under all the three RCPs. The increase is most evident under RCP4.5. Most of the individual

models yield a consistent result with MME. For OFC, seven, eight and six models among all the eleven models project the result consistent with MME under RCP2.6, RCP4.5 and RCP8.5, respectively. The numbers are eight, eight and six for TRD.

In fall (Figs. 4c and 4d), a significantly reversed decrease trend is projected in OFC and TRD. The higher the emission, the more obvious the decrease is. As for individual models, for OFC, a total of three, three and five models among all the five "good" models project a decrease under RCP2.6, RCP4.5 and RCP8.5, respectively. The number is two, three and five for TRD.

In view of regional difference in CREs within TGR from south to north (Zheng et al., 2018), whether the CREs trends vary in different subregions is intriguing. Figure 5a shows the distribution of projected spring OFC and TRD trend in MME. A resemblance is seen between them. First there is an overall increase in the whole region, particularly its plain western section. Second, the increase is more visible under the lower emissions (RCP2.6 and RCP4.5) than the higher emission (RCP8.5). This has been seen in the area mean above.

Since the result from one single model may dominate MME, this causes uncertainty of projected results. To assess the uncertainty, we analyze the agreement of the models' results. Figure 5b displays the spatial distribution of model number projecting an increase in occurrence of CREs. From it, most of models show a positive trend in OFC and TRD (warm yellow corresponds to an upward trend) in spring. Also, more models are in agreement with MME in the western section. This indicates a larger reliability in the CRE increase there (Fig. 5a).

The distribution of projected trend in occurrence MME in fall is displayed in figure 6a. A decrease both in OFC and TRD is seen across the area, particularly over the southwestern section. The decrease is even obvious under the higher emission scenario. This is also seen from the distribution of the number of model (Fig. 6b). The number of models is represented with deeper blue when they project an overall downward trend in OFC and TRD (Figs. 4c and 4d). The southwestern section of TGR projects a consistent decrease under all three scenarios, where CREs occur most frequently in fall (Zou, 2005). Besides, the models' agreement increases along with the enhancement of emissions. Almost all the five "good" models project a reduction trend in occurrence across the region under RCP8.5, and the reduction in about one half of the models is significant in these grid points.

4.2 *Intensity*

Strong precipitation increases the risk of geological hazards (Corominas and Moya, 1999; Guzzetti et al., 2007; Jibson, 2006). Here we analyze the projected intensity of CREs expressed as ACR and INT. From figure 7 (right to the vertical black dashed line), a significant increase in ACR and INT in spring is seen under all three RCP scenarios. The higher the emission, the more evident the increase is. During 2070-2099, ACR is projects to increase by 19.4%, 29.2% and 30.8% under RCP2.6, RCP4.5 and RCP8.5, respectively, relative to 1970-1999. The values for INT are 11.9%, 16.6% and 25.7 %. Also, most of the model bear a consistent projection with MME. The number of the models is nine, ten and eight for ACR under RCP2.6,

RCP4.5 and RCP8.5 respectively. This number is eight, eleven and eleven for INT, respectively.

In fall (Figs. 7c and 7d), a negative trend in ACR is projected, being significant under RCP4.5 and RCP8.5. There is (are) one, three and three model(s) among the five “good” models projecting the result consistent with MME under RCP2.6, RCP4.5 and RCP8.5, respectively. That only one model bears a similar projection to MME implies substantial uncertainty under RCP2.6. For INT, one opposite result is projected, but it may be robust since four, three and five models among all the five “good” models yield a result similar to MME.

Figure 8a shows the spatial distribution of projected spring ACR and INT trend in MME. ACR under all three scenarios shows an increase from north to south, while INT increases in different sections under different emissions. Under the lower scenario, the increase is located in the highly-populated southwestern section, but in the northeastern closer to the Great Dam under the higher emissions. The model’s spread is checked in Figure 8b. For ACR, almost all models project a positive trend under all the three scenarios, particularly in the southwestern section. A greater spatial homogeneity is seen in INT under RCP4.5 and RCP8.5 than that under RCP2.6.

The spatial distribution of projected fall ACR and INT trend in MME is displayed in Figure 9a. Similar to occurrence (Figure 6a), a decrease in ACR is located in the southwestern area, and it is more pronounced under the higher scenario. INT shows an increase in the western section under RCP2.6 and RCP8.5, but a decrease across the area under RCP4.5. Similar to the previous analyses, the model

404 number projecting a same trend as MME is presented in figure 9b. From it, the
405 models' agreement is relatively higher in ACR under higher than lower emissions.

406 Both the accumulated amount and short-duration rainstorm intensity are crucial
407 triggering geological hazards (Corominas and Moya, 1999; Jibson, 2006). Thus, an
408 in-depth analysis on ACR and INT in individual models is conducted below. Figure
409 10 shows the frequency distribution of spring ACR bins for different decades under
410 RCP 4.5. In spite of an in-between difference, most of the models yield a visible
411 increase in the future. For example, there is an increased frequency of heavy ACR
412 (exceeding 80 mm) during 2070 to 2099 in CNRM-CM5, HadGEM2-AO,
413 HadGEM2-ES and MRI-CGCM3. Also, the increase in spring under different
414 scenarios is similar to one another, but with a greater amplitude under RCP8.5 than
415 RCP2.6. In fall, the individual models project a regional non-unanimous result except
416 for CNRM-CM5, which projects increased grids with ACR exceeding 200 mm during
417 the late 21st century. There is no significant change in the two models from IPSL but
418 a slight decrease from the two models else.

419 The increase in evaporation resulted by warming is greater than the atmospheric
420 capacity in holding moisture, this imbalance implicates a decrease in light to moderate
421 precipitation events (Sun, 2006; Trenberth, 1998). The light to moderate precipitation
422 events consiste of a fraction of CREs. To obtain the projection of precipitation
423 intensity in CREs (i.e. INT) in the future, the 90th, 95th and 99th percentiles obtained
424 by aggregating daily rainfall intensity from all CREs are used to classify four major
425 categories: light rainy (LR), moderate rainy (MR), heavy rainy (HR), and extreme

426 rainy (ER) days. Figure 11 compares the projected change in the individual models in
427 2020-2049 (near-future) and 2070-2099 (far-future) relative to 1970-1999. In
428 far-future, for spring LR (Fig. 11b) there is about a half of the models projecting a
429 reduction but an increase by the remaining models. For spring MR, more models
430 project an increase with a higher model agreement. Also, almost all models project an
431 increased HR and ER, and this is particularly evident by HadGEM2-ES,
432 HadGEM2-AO, and MRI-CGCM3. Besides, the increase is most significant under
433 high emissions. In fall, for LR, MR and HR, most models project weakening in daily
434 rainfall intensity, and the weakening is most prominent under all three scenarios in
435 MRI-CGCM3. In contrast, all the models display an enhanced daily intensity in ER
436 under RCP 2.6 and RCP 8.5.

437 In near-future the projected changes (Fig. 11a) are qualitatively similar to the
438 far-future but weaker. This indicates a gradual increase in spring daily rainfall
439 intensity during CREs in the future (Fig. 7b). In fall an overall increase is projected
440 (Fig. 7d), although it is not so unanimous in different categories. This increase may be
441 attributed to the growth of ER events. This seems reasonable because the precipitable
442 water within the atmosphere increases under a warming context, and it is easier to
443 form bigger particles and rain drops.

444

445 ## 5. Summary and discussions

446 The Three Gorges Reservoir area (TGR) in China suffers from geological
447 hazards like landslide downhill and mudslide. Consecutive rainfall event (CRE) is a

448 substantial trigger. In this study we used the IPCC CMIP5 outputs to project the future
449 trends of CREs' occurrence and intensity. Just the "good" models are chosen to
450 project based on their historical simulations on the observed CREs.

451 Considering the common systemic bias with more rainy days in most of the
452 state-of-the-art models, a new approach to defining model's rainy days has been
453 developed based on the Cumulative probability Distribution Function of the observed
454 daily rainfall amount. Then, models' rainy days number has been derived to identify
455 CREs. A total of eleven /five models have been selected as "good" models to project
456 the future trends for spring /fall. These models have exhibited a relatively higher skill
457 in reproducing observed CREs' spatial patterns and interannual variability of
458 occurrence.

459 The results suggest an increase of the occurrence of CREs in spring, being most
460 significant under RCP4.5, but a reduction in fall, being more evident under higher
461 scenarios. The projected change in occurrence is more prone in the southern and
462 western sections of the area. The projected change in accumulated rainfall amount is
463 similar to the occurrence in both seasons. In contrast to difference in occurrence
464 between the two seasons, the projected daily rainfall intensity in CREs increases
465 overall in both spring and fall. The projected increase in occurrence and/or
466 intensifying in daily rainfall intensity imply a higher risk of geological hazards in
467 TGR in future.

468 It has been well known that CREs occur under a more stable and
469 longitudinally-oriented circulation pattern dominated with blocking at mid-high

latitudes (Ding et al., 2008; Luo et al., 2013). In the recent decades, the Arctic warms much faster than the mid-lower latitudes, the weakening of the north-south temperature gradient causes a reduction in the atmospheric baroclinicty and subsequently weakens the mid-latitudinal westerly and a much broader meridional meanders in mid-high latitudes (Liu et al., 2012; Outten and Esau, 2012). The change might affect the atmospheric pattern pattern related to CREs. From figure 12, the spring geopotential height has increased obviously in east Siberia but not in the Ural region through 1960-2018. In fall, a prominent increase occurs in the Barents Sea region. Such a difference in atmospheric circulation trend between the two seasons may have contributed their opposite trend in CREs' occurrence.

Here just the statistical downscaling scheme based on GCM outputs is used. In addition to the statistical downscaling, the dynamical downscaling with regional climate models is also an effective approach. It bears more physical meaning. Projecting the future trend of CREs in regional climate model like WRF consists of our future work.

There exists some uncertainty in the present study. First, climate simulations have larger uncertainty over mountainous areas like TGR than over plain basins (Palazzi et al., 2013, 2015). Precipitation is much more poorly simulated than other variables such as air temperature, due to its strong localization, relatively sparse instrument samples as well as the weaker physical constraints (Allen and Ingram, 2002). Also, the observational gridded dataset used here, CN05.1, embraces uncertainty due to the adapted interpolation. Besides, the coarse spatial resolution of

the CMIP5 models is also one major source of uncertainties (Birkinshaw et al., 2017). Finally, just several models (IPSL-CM5A-LR, IPSL-CM5A-MR, CNRM-CM5, MRI-CGCM3, CSIRO-Mk3.6.0) analyzed here incorporate the direct effects and the first indirect effects of aerosols, this affects definitely the identification and projection of CREs since aerosols are essential for precipitation frequency (Jing et al., 2017). This is another source of uncertainty.

Acknowledgments

The data that support the findings of this study are listed below. Original station gauged data of CN05.1 can be obtained at a Chinese website http://data.cma.cn/data/cdcdetail/dataCode/SURF_CLI_CHN_MUL_DAY_V3.0.html after registration, and relevant English information can be found at http://data.cma.cn/en/?r=data/detail&dataCode=SURF_CLI_CHN_MUL_DAY_CES_V3.0. CMIP5 model outputs are available at website https://esgf-node.llnl.gov/search/cmip5/.

Appendix: Abbreviation in the context

Abbreviated Index	Full name
CREs	Consecutive Rainfall Events
TGR	The Three Gorges Reservoir area
RCP	Representative Concentration Pathways
MME	Multiple-model ensemble mean
OCF	Occurrence frequency
TRD	Total rainy days
ACR	Accumulated rainfall amount
INT	Mean rainfall intensity

References

Allen, M. R., & Ingram, W. J. (2002). Constraints on future changes in the hydrological cycle. *Nature*, 419(6903), 228-232. https://doi.org/10.1038/nature01092

Birkinshaw, S. J., Guerreiro, S. B., Nicholson, A., Liang, Q., & Fowler, H. J. (2017). Climate change impacts on yangtze river discharge at the three gorges dam. *Hydrology and Earth System Sciences*, 21(4), 1911-1927. https://doi.org/10.5194/hess-21-1911-2017

Boé, J., Terray, L., Habets, F., & Martin E. (2007). Statistical and dynamical downscaling of the seine basin climate for hydro-meteorological studies. *International Journal of Climatology*, 27(12), 1643-1655. https://doi.org/10.1002/joc.1602

Chen, G., Sha, W., Iwasaki, T., & Ueno, K. (2012). Diurnal variation of rainfall in the Yangtze River Valley during the spring‐summer transition from TRMM measurements. *Journal of Geophysical Research Atmospheres*, 117, D06106. https://doi.org/10.1029/2011JD017056

Chen, X., Xu, Y., Xu, C., & Yao, Y. (2014). Assessment of precipitation simulations in China by CMIP5 multi-models. *Progressus Inquistitiones De Mutatione Climatis*, 10(3). https://doi.org/10.3969/j.issn.1673-1719.2014.03.011

Corominas, J., & Moya, J. (1999). Reconstructing recent landslide activity in relation to rainfall in the Llobregat River basin, Eastern Pyrenees, Spain. *Geomorphology*, 30(1-2), 79-93. https://doi.org/10.1016/S0169-555X(99)00046-X

536 Dai, A., & Trenberth, K. E. (2004). The diurnal cycle and its depiction in the
537 community climate system model. *Journal of Climate*, 17(5), 930-951.
538 https://doi.org/10.1175/1520-0442(2004)017<0930:TDCAID>2.0.CO;2
539 Déqué, M. (2007). Frequency of precipitation and temperature extremes over France
540 in an anthropogenic scenario: model results and statistical correction according
541 to observed values. *Global and Planetary Change*, 57(1-2), 16-26.
542 https://doi.org/10.1016/j.gloplacha.2006.11.030.
543 Ding, Y., Wang, Z., Song, Y., & Zhang, J. (2008). The Unprecedented Freezing
544 Disaster in January 2008 in Southern China and Its Possible Association with the
545 Global Warming. *Journal of Meteorological Research*, 22(4), 538-558.
546 Fang, G., Yang, J., Chen, Y., & Zammit, C. (2015). Comparing bias correction
547 methods in downscaling meteorological variable for a hydrologic impact study in
548 an arid area in China. *Hydrology and Earth System Sciences*, 19, 2547-2559.
549 https://doi.org/10.5194/hess-19-2547-2015.
550 Giorgi, F., Coppola, E., Raffaele, F., Diro, G. T., Fuentes-Franco, R., Giuliani, G., &
551 Torma, C. (2011). Higher hydroclimatic intensity with global warming. *Journal*
552 *of Climate*, 24, 5309-5324. https://doi.org/10.1175/2011JCLI3979.1
553 Giorgi, F., Whetton, P. H., Jones, R. G., Christensen, J. H., Mearns, L. O., Hewitson
554 B., vonStorch, H., Francisco, R. & Jack, C. (2001). Emerging patterns of
555 simulated regional climatic changes for the 21st century due to anthropogenic
556 forcings. *Geophysical Research Letters*, 28(17), 3317-3320.
557 https://doi.org/10.1029/2001GL013150

Gotway, C. A. (1992). Statistical Methods in Water Resources. *Technometrics*, 36, 323-324, https://doi.org/10.1080/00401706.1994.10485818

Guzzetti, F., Peruccacci, S., Rossi, M., & Stark, C. P. (2007). Rainfall thresholds for the initiation of landslides in Central and Southern Europe. *Meteorology and Atmospheric Physics,* 98(3-4), 239-267. https://doi.org/10.1007/s00703-007-0262-7

Han, L., Han, Z., & Li, S. (2014). Projection of heavy rainfall events in the middle and lower reaches of the Yangtze River valley in the 21st century under different representative concentration pathways. *Transactions of Atmospheric Sciences,* 37(5), 529-540. https://doi.org 10.13878/j.cnki.dqkxxb.20130512001

Hung, N., Babel, M. S., Weesakul, S., & Tripathi, N. K. (2009). Tripathi.An artificial neural network model for rainfall forecasting in Bangkok, Thailand. *Hydrology and Earth System Sciences*, 13, 1413-1425.

Jibson, R. W. (2006). The 2005 La Conchita, California, landslide. *Landslides*, 3(1), 73-78. https://doi.org/10.1007/s10346-005-0011-2

Jing, X., Suzuki, K., Guo, H., Goto, D., Ogura, T., Koshiro, T., & Mülmenstädt, J. (2017). A Multimodel Study on Warm Precipitation Biases in Global Models Compared to Satellite Observations. *Journal of Geophysical Research Atmospheres*, 21, 806-824. https://doi.org/10.1002/2017JD027310

Lau, K. M., Wu, H., & Kim, K. M. (2013). A canonical response of precipitation characteristics to global warming from CMIP5 models. *Geophysical Research Letters*, 40, 3163-3169. https://doi.org/10.1002/grl.50420, 2013

Li, H., Chen, H., Sun, B., Wang, H., & Sun, J. (2020). A Detectable Anthropogenic Shift Toward Intensified Summer Hot Drought Events Over Northeastern China. *Earth and Space Science*, 7, e2019EA000836. https://doi.org/10.1029/2019EA000836

Li, M., Pan, J. & Tian, S. (1977). Forecast Method of Continuous Low Temperature and Rainy Weather in Spring, Beijing, Science Press.

Li, W., Jiang, Z., Xu, J., & Li, L. (2016). Extreme Precipitation Indices over China in CMIP5 Models. Part II: Probabilistic Projection. *Journal of Climate*, 24, 8989-9004. https://doi.org/10.1175/jcli-d-16-0377.1

Liu, C. (2015). Landslide disaster in Lidong Village, Yaxi Town, Liandu District, Lishui City, Zhejiang Province. *The Chinese Journal of Geological Hazard and Control*, 4, 5-5.

Liu, J., Curry, J. A., Wang, H., Mirong, S., & Radley M. H. (2012). Impact of declining Arctic sea ice on winter snowfall. *Proceedings of the National Academy of Sciences*, 109(11), 4074-4079. https://doi.org/1073/pnas.1114910109

Luk, K. C., Ball, J. E., Sharma, A. (2000). A study of optimal model lag and spatial inputs to artificial neural network for rainfall forecasting. *Journal of Hydrology*, 227(1-4), 56-65. https://doi.org/10.7522/j.issn.1000-0534.2013.00018

Luo, X., Li, D., & Wang, H. (2013). New Evolution Features of Autumn Rainfall in West China and Its Response to Atmospheric Circulation. *Plateau Meteorology*, 32(4), 1019-1031. https://doi.org/10.7522/j.issn.1000-0534.2013.00018

602 Ma, Z., Zhang, Q., Zhu, R., & Jiang, Z. 2005: The Basic Characters of Mountain
603 Disasters and Relationship between Landslide and Rainfall in the Area of
604 Three-Gorge Reservoir. *Journal of Catastrophology*, 23(3), 319-326.
605 https://doi.org/10.3969/j.issn.1008-2786.2005.03.011
606 Ma, Z., Zhu, R., & Zhang, Q. (2006). Numerical simulation of severe precipitation in
607 Three-gorge Reservoir area and its application to landslide forecast. *Journal of*
608 *Natural Disasters*, 19, 1044-1052.
609 Mendes, D., & Marengo, J. A. (2010). Temporal downscaling: a comparison between
610 artificial neural network and autocorrelation techniques over the Amazon Basin
611 in present and future climate change scenarios. *Theoretical and Applied*
612 *Climatology*, 100(3), 413-421. https://doi.org/10.1007/s00704-009-0193-y
613 Mohan, S. T., & Rajeevan, M. (2017). Past and future trends of Hydroclimatic
614 Intensity over the Indian Monsoon Region. *Journal of Geophysical Research*
615 *Atmospheres*, 122(2), 896-909. https://doi.org/10.1002/2016JD025301
616 New, M., Hulme, M., & Jones, P. (2000). Representing twentieth-century space-time
617 climate variability. part ii: development of 1901-96 monthly grids of terrestrial
618 surface climate. *Journal of Climate*, 13(13), 2217-2238.
619 https://doi.org/10.1175/1520-0442(2000)013<2217:RTCSTC>2.0.CO;2
620 Outten, S. D., & Esau, I. (2012). A link between Arctic sea ice and recent cooling
621 trends over Eurasia. *Climatic Change*, 110(3), 1069-1075.
622 https://doi.org/10.1007/s10584-011-0334-z
623 Palazzi, E., Hardenberg, J. V., & Provenzale, A. (2013). Precipitation in the

624 Hindu-Kush Karakoram Himalaya: Observations and future scenarios. *Journal of*
625 *Geophysical Research Atmospheres*, 118(1), 85-100,
626 https://doi.org/10.1029/2012JD018697
627 Palazzi, E., Hardenberg, J. V., Terzago, S., & Provenzale, A. (2015). Precipitation in
628 the Karakoram-Himalaya: a CMIP5 view. *Climate Dynamics.*, 45(1-2), 21-45.
629 https://doi.org/10.1007/s00382-014-2341-z
630 Pan, X. D., Zhang, L., & Huang, C. L. (2020). Future climate projection in Northwest
631 China with RegCM4.6. *Earth and Space Science*, 7, e2019EA000819.
632 https://doi.org/10.1029/2019EA000819
633 Salinger, M. J., & Griffiths, G. M. (2001). Trends in New Zealand daily temperature
634 and rainfall extremes. *International Journal of Climatology*, 21(12), 1437-1452.
635 https://doi.org/10.1002/joc.694
636 Santer, B. D., Taylor, K. E., Gleckler, P. J., & Bonfils, C. (2009). Incorporating model
637 quality information in climate change detection and attribution studies.
638 *Proceedings of the National Academy of Sciences*, 106(35), 14778-14783.
639 https://doi.org/10.1073/pnas.0901736106
640 Santos, M., & Fragoso, M. (2013). Precipitation variability in Northern Portugal: Data
641 homogeneity assessment and trends in extreme precipitation indices.
642 *Atmospheric Research*, 131, 34-45.
643 https://doi.org/10.1016/j.atmosres.2013.04.008
644 Schmidli, J., Frei, C., & Vidale, P. L. (2006). Downscaling from GC precipitation: A
645 benchmark for dynamical and statistical downscaling methods. *International*

Journal of Climatology, 26(5), 679-689. https://doi.org/10.1002/joc.1287

Scoccimarro, E., & Gualdi, S. (2013). Heavy precipitation events in a warmer climate: results from CMIP5 models. *Journal of Climate*, 26(20), 7902-7911. https://doi.org/10.1175/JCLI-D-12-00850.1

Semenov, M. A., & Stratonovitch, P. (2010). Use of multi-model ensembles from global climate models for assessment of climate change impacts. *Climate Research*, 41(1), 1-14. https://doi.org/10.3354/cr00836

Sen, P. K. (1968). Estimates of the Regression Coefficient Based on Kendall's Tau. *Publications of the American Statistical Association*, 63(324), 1379-1389. https://doi.org/10.1080/01621459.1968.10480934

Sillmann, J., Kharin, V. V., Zwiers, F. W., & Zhang, X. (2013). Climate extremes indices in the CMIP5 multimodel ensemble: Part 2: Future climate projections. *Journal of Geophysical Research Atmospheres*, 118(6), 2473-2493. https://doi.org/10.1002/jgrd.50188

Skamarock, W. C., Klemp, J. B., & Dudhia, J. (2008). A Description of the Advanced Research WRF Version 3. Boulder, CO, USA, National Center for Atmospheric Research Technical Note.

Sui, Y., Lang, X. & Jiang, D. (2015). Temperature and precipitation signals over China with a 2°C global warming. *Climate Research*, 64(3), 227-242. https://doi.org/10.3354/cr01328

Sun, Y., Solomon, S., Dai, A., & Portmann, R. W. (2006). How often does it rain? *Journal of Climate*, 19(6), 916-934. https://doi.org/10.1175/JCLI3672.1

668 Sun, Y., Solomon, S., Dai, A., & Portmann, R. W. (2007). How Often Will It Rain?
669 *Journal of Climate*, 20, 4801-4818. https://doi.org/10.1175/JCLI4263.1
670 Sun, Z., Huang, Y. & Ni, D. (2016). Climate and circulation characteristics of
671 continuous autumn rain in China. *Transactions of Atmospheric Sciences*, 39(4),
672 480-489. https://doi.org/10.13878/j.cnki.dqkxxb.20140413001.
673 Taylor, K. E. (2001). Summarizing multiple aspects of model performance in a single
674 diagram. *Journal of Geophysical Research Atmospheres*, 106(D7), 7183-7192.
675 https://doi.org/10.1029/2000JD900719
676 Taylor, K. E., Stouffer, R. J., & Meehl, G. A. (2012). An Overview of CMIP5 and the
677 Experiment Design. *Bulletin of the American Meteorological Society*, 93(4),
678 485-498. https://doi.org/10.1175/BAMS-D-11-00094.1
679 Teutschbein, C., & Seibert, J. (2012). Bias correction of regional climate model
680 simulations for hydrological climate-change impact studies: Review and
681 evaluation of different methods. *Journal of Hydrology*, 456, 12-29.
682 https://doi.org/10.1016/j.jhydrol.2012.05.052
683 ThemeßL, M. J., Gobiet, A., & Heinrich, G., (2012). Empirical-statistical
684 downscaling and error correction of regional climate models and its impact on
685 the climate change signal. *Climatic Change*, 112(2), 449-468.
686 https://doi.org/10.1007/s10584-011-0224-4
687 Trenberth, K. E. (1998). Atmospheric Moisture Residence Times and Cycling:
688 Implications for Rainfall Rates and Climate Change. *Climatic Change*, 39(4),
689 667-694. https://doi.org/10.1023/A:1005319109110

690 Wang, R., & Zou, X. (2015). An analysis on the change characterisitics of
691 consecutive rainfall in the middle and lower reaches of the Yangtze River.
692 *Resources and Environment in the Yangtze Basin*, 24(9), 1483-1490, doi:
693 10.11870/cjlyzyyhj201509007
694 Wang, X. L., & Swail, V. R. (2001). Changes of Extreme Wave Heights in Northern
695 Hemisphere Oceans and Related Atmospheric Circulation Regimes. *Journal of*
696 *Climate*, 14(10), 2204-2221.
697 https://doi.org/10.1175/1520-0442(2001)014<2204:COEWHI>2.0.CO;2
698 Wu, J., & Gao, X. (2013). A gridded daily observation dataset over China region and
699 comparison with the other datasets. *Chinese Journal of Geophysics*, 56(4),
700 1102-1111. https://doi.org/10.6038/cjg20130406
701 Xu, Y., Gao, X., Shen, Y., & Xu, C. (2009). A daily temperature dataset over China
702 and its application in validating a RCM simulation. *Advances in Atmospheric*
703 *Sciences*, 26(4), 763-772. https://doi.org/10.1007/s00376-009-9029-z
704 Ye, D., Zhang, Q., Zou, X., & Chen, X. (2009). Changing trends of major
705 meteorological disasters in recent dacades over gorges reservorir area. *Resources*
706 *and Environment in the Yangtze Basin*, 18(3), 296-300.
707 https://doi.org/10.3969/j.issn.1004-8227.2009.03.017
708 Yue, S., Pilon, P., Phinney, B., & Cavadias, G. (2002). The influence of
709 autocorrelation on the ability to detect trend in hydrological series. *Hydrological*
710 *Processes*, 16(9), 1807-1829. https://doi.org/10.1002/hyp.1095
711 Zhai, P. (1999). Detection of trends in China's precipitation extremes. *Acta*

Meteorologica Sinica, 25(1), 5-8.

Zhang, J., Ying, K., Wang, J., & Liu, L. (2016). Evaluation of landslide susceptibility for Wanzhou district of Three Gorges Reservoir. *Chinese Journal of Rock Mechanics and Engineering*, 35, 20-20. https://doi.org/10.13722/j.cnki.jrme.2015.0318

Zheng, Y., Li, S., & Zhang, C. (2018). Climatic trend analysis of consecutive rainfall events over Three Gorges Reservoir Area in spring. *Torrential Rain and Disasters*, 37, 1-6. https://doi.org/10.3969/j.issn.1004-9045.2018.04.009

Zou, X. (2005). An Analysis on the Climatic Characteristics of Consecutive Rainfall in the Three Gorges Area. *Journal of Catastrophology*, 20, 84-89. https://doi.org/10.1360/biodiv.050028

724 Table 1 Details of the 20 CMIP5 models

ID	Model name	Institute (Institude ID)	Lat×Lon(degrees)
1	BCC-CSM1.1	Beijing Climate Center, China Meteorological Administration (BCC)	~2.8×~2.8
2	BNU-ESM	College of Global Change and Earth System Science, Beijing Normal University (GCESS)	~2.8×~2.8
3	FGOALS-g2	Institute of Atmospheric Physics, Chinese Academy of Sciences (LASG-IAP)	~2.8×~2.8
4	IPSL-CM5A-LR	Institut Pierre Simon Laplace (IPSL)	~1.9×3.75
5	IPSL-CM5A-MR		~1.25×2.5
6	CNRM-CM5	Centre National de Recherches Meteorologiques-Centre Europeen de Recherche et Formation Avancees en Calcul Scientifique (CNRM- CERFACS)	~1.4×~1.4
7	CanESM2	Canadian Center for Climate Modelling and Analysis (CCCMA)	~2.8×~2.8
8	GFDL-CM3	NOAA Geophysical Fluid Dynamics Laboratory (NOAA GFDL)	~2×2.5
9	GFDL-ESM2G		~2×2.5
10	GFDL-ESM2M		~2×2.5
11	HadGEM2-AO	Met Office Hadley Centre (MOHC)	1.25×~1.9
12	HadGEM2-ES		1.25×~1.9
13	MIROC-ESM	National Institute for Environmental Studies,The University of Tokyo (MIROC)	~2.8×~2.8
14	MIROC-ESM-CHEM		~2.8×~2.8
15	MIROC5		~1.4×~1.4
16	MPI-ESM-LR	Max Planck Institute for Meteorology (MPI-M)	~1.9×~1.9
17	MPI-ESM-MR		~1.9×~1.9
18	MRI-CGCM3	Meteorological Research Institute (MRI)	~1.1×~1.1
19	NorESM1-M	Norwegian Climate Centre (NCC)	~1.9×2.5
20	CSIRO-Mk3.6.0	Commonwealth Scientific and Industrial Research Organization in collaboration with Queensland Climate Change Centre of Excellence (CSIRO-QCCCE)	~1.9×~1.9

725

726

727

728 Table 2 One comparison of the threshold, modeled seasonal rainfall, averaged
729 magnitude and trend (per decade) of CREs in the historical runs of the “good” models
730 with those in observation. The four variables (OCF, TRD, ACR and INT) are used to
731 describe CREs, and CREs are identified by threshold based on the new approach. “ * ”
732 indicates significant at the 95% confidence level. See the context.

ID	Models	Spring									
		Thres.	Seasonal Rainfall	OCF		TRD		ACR		INT	
				Mag.	Trend	Mag.	Trend	Mag.	Trend	Mag.	Trend
	CN05.1	1	328.1	2.0	-0.10	18.1	-0.83	143.1	-11.82	7.8	-0.28*
3	FGOALS-g2	3.5	352.6	1.9	0.03	19.3	0.21	157.5	4.93	8.1	0.10
4	IPSL-CM5A-LR	1	276.2	2.1	0.01	18.9	-0.78	122.3	-3.42	6.5	0.05
5	IPSL-CM5A-MR	0.7	274.0	2.0	0.00	19.1	0.01	125.3	-1.37	6.6	-0.07
6	CNRM-CM5	3.1	379.4	2.0	-0.03	20.3	0.64	187.5	5.15	9.2	0.02
7	CanESM2	3	444.0	2.0	0.07	20.5	1.21	221.3	15.30	10.8	0.07
11	HadGEM2-AO	3.7	455.7	2.0	-0.02	18.9	-0.43	229.7	-5.61	12.2	-0.08
12	HadGEM2-ES	3.7	421.3	2.1	-0.09	18.4	-0.54	203.3	5.83	11.1	0.33*
15	MIROC5	3	462.8	2.0	-0.05	17.7	-0.68	192.5	-5.61	10.8	0.18
16	MPI-ESM-LR	3.2	454.8	2.0	0.05	18.4	0.02	195.9	5.12	10.6	0.38*
18	MRI-CGCM3	2.1	355.7	2.0	-0.09	19.9	-0.77	161.9	-8.65	8.0	-0.05
20	CSIRO-Mk3.6.0	2.1	375.0	2.0	-0.02	20.0	-0.08	176.9	-1.36	8.9	0.05
G	MME_G			2.0	0.01	19.2	-0.02	179.5	1.13	7.9	0.03
A	MME_A			2.1	0.00	19.7	-0.03	190.7	0.43	8.6	-0.02
		Fall									
		Thres.	Seasonal Rainfall	OCF		TRD		ACR		INT	
				Mag.	Trend	Mag.	Trend	Mag.	Trend	Mag.	Trend
	CN05.1	1	250.3	2.0	-0.24*	18.6	-2.90*	148.6	-27.42*	7.9	-0.18
4	IPSL-CM5A-LR	0.7	227.9	2.3	-0.20*	22.2	-1.92	155.8	-13.78	6.9	-0.10
5	IPSL-CM5A-MR	0.1	163.0	2.4	-0.16	25.2	-2.45	121.6	-14.2*	4.8	-0.04
6	CNRM-CM5	1.7	255.5	2.4	-0.04	22.0	-0.82	154.5	-2.73	7.0	0.06
18	MRI-CGCM3	1	239.2	2.2	-0.09	21.0	-1.19	137.5	-4.49	6.4	0.10
20	CSIRO-Mk3.6.0	0.5	190.4	2.3	-0.32*	22.1	-3.22*	129.6	-20.78*	5.7	-0.01
G	MME_G			2.3	-0.14*	22.5	-1.40*	139.8	-9.38*	5.8	-0.09
A	MME_A			2.2	-0.08*	21.9	-0.97*	167.8	-7.13*	7.0	-0.08

733

734

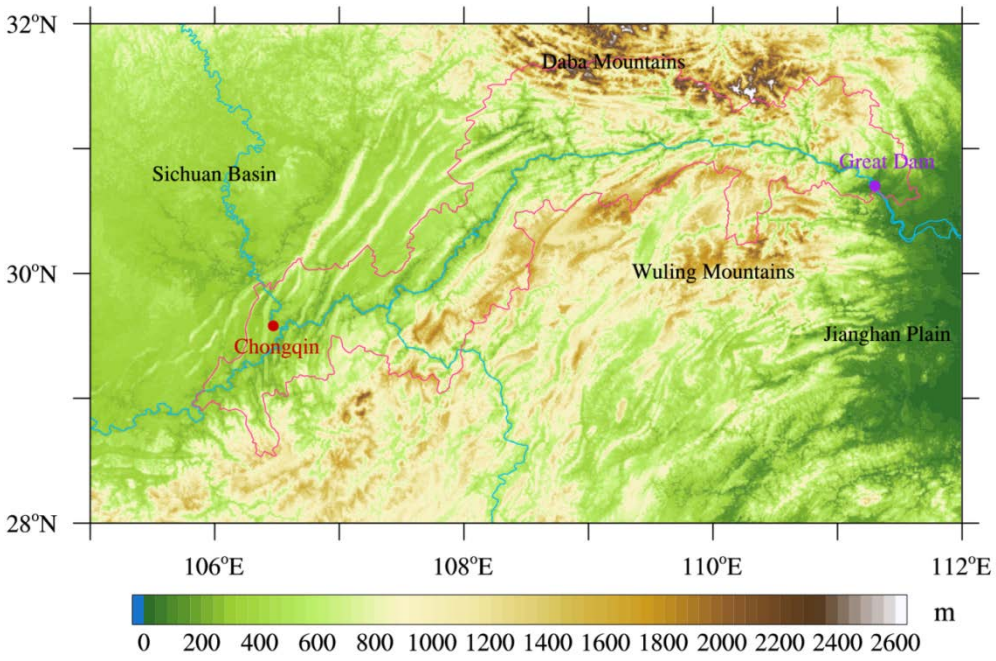

Figure 1 The topography distribution of the TGR. The west and east sections to TGR are the Sichuan Basin and the Jianghan Plain, and the north and south sections to TGR are the Daba Mountains and the Wuling Mountains, respectively. The red dot of upstream is Chongqing City, which is a provincial capital with a population of 30 million, and the purple dot of the downstream indicates the location of the Great Dam of TGR.

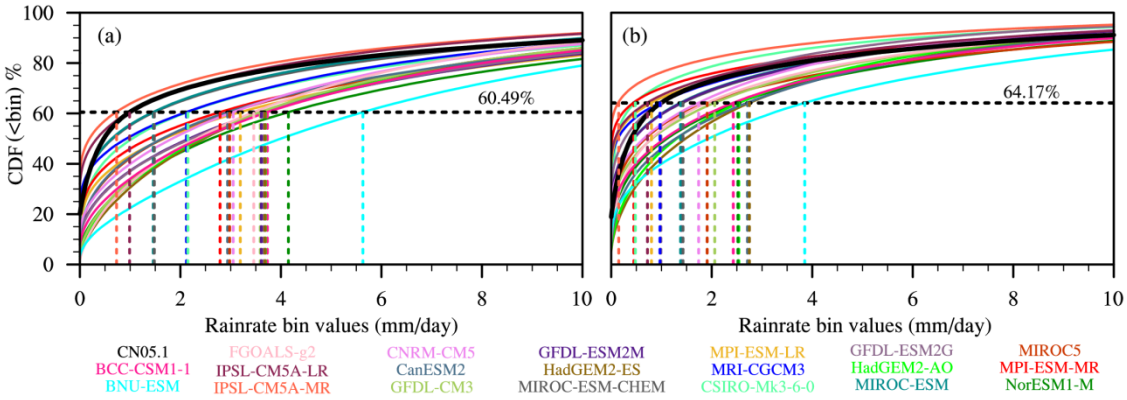

Figure 2 The CDF of daily rainfall amount in (a) spring and (b) fall based on CN05.1 and twenty CMIP5 models. The colorful curves represent different models and the black curve represents the observation (CN05.1). The black horizontal dashed line represents the CDF of observed daily rainfall with the amount over 1 mm threshold, and the color vertical dashed lines correspond to the model threshold at horizontal axis.

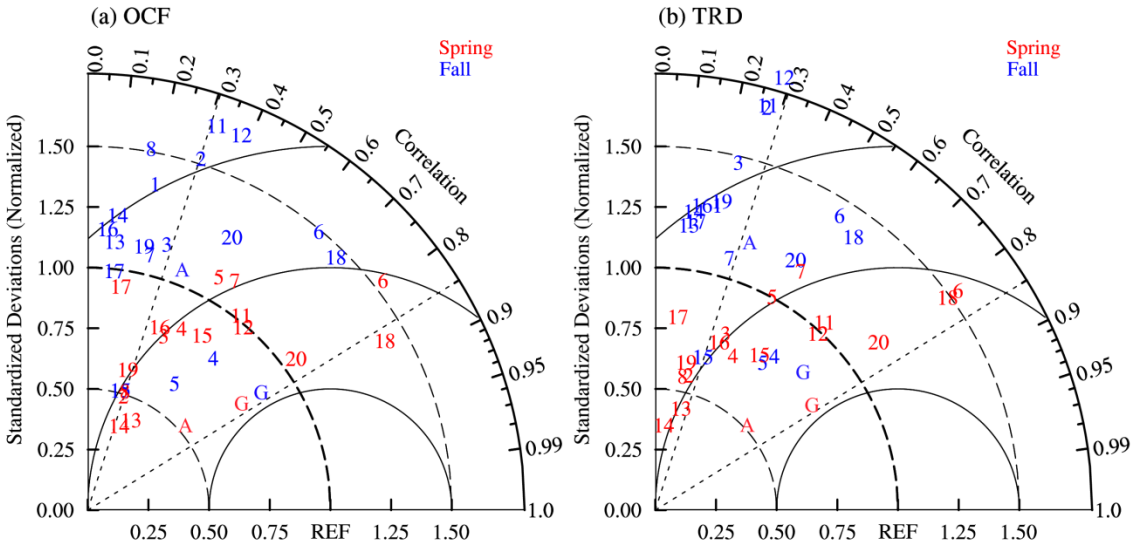

Figure 3 Taylor diagram displaying normalized pattern statistics of climatological seasonal mean (a) OCF and (b) TRD (models with a negative correlation coefficient, large root-mean-square difference or large standard deviation are not shown). Each number represents a model ID (see Table 1). The reference (REF) indicates observation from CN05.1. Red and blue denote the spring and fall, respectively. The correlation coefficient between a model and the CN05.1 is given by the azimuthal position, with oblique dotted lines showing the 95% confidence level. The normalized standard deviation of a model is the radial distance from the origin, with cambered thick dashed lines showing the value of 1.0 and cambered thin dashed lines showing the value of 0.5 and 1.5, respectively. The normalized centered RSM difference between a model and the reference is their distance apart, with cambered solid lines at intervals of 0.5.

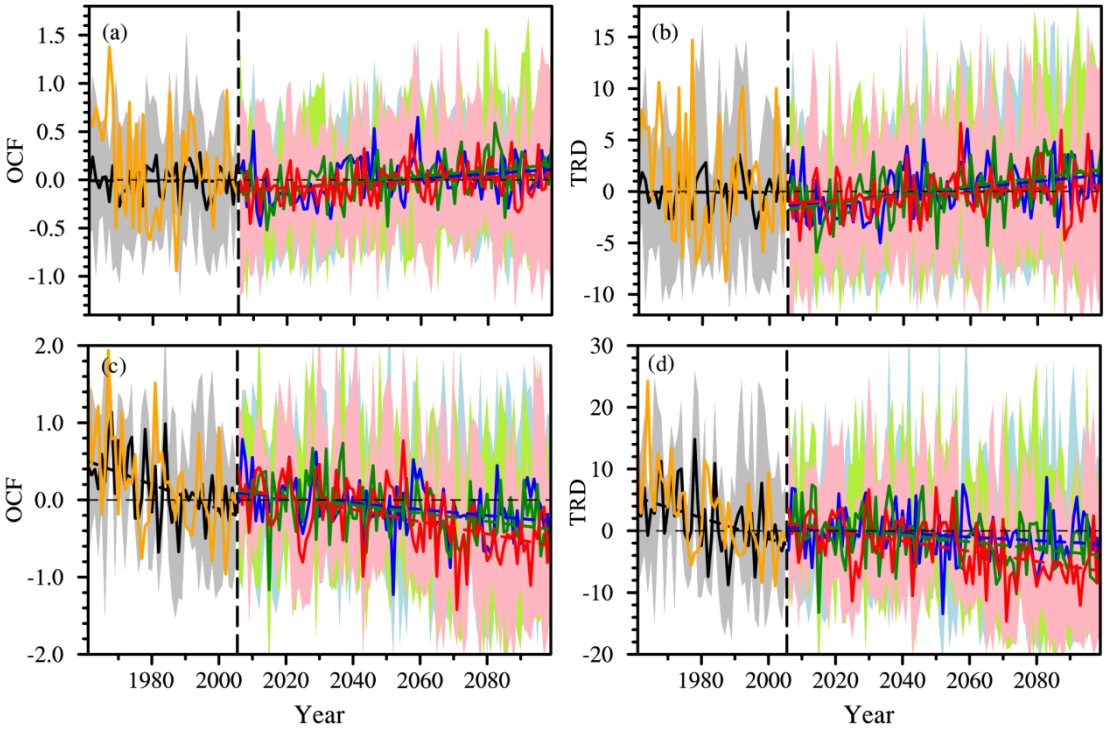

Figure 4 Temporal evolution of simulated OCF and TRD in spring ((a) and (b)) and fall ((c) and (d)) in CMIP5 historical runs (left to the vertical black line in each panel) and projected runs (right to the vertical black line). For the historical period (1961-2005), yellow and black lines represent the observed and MME simulated, respectively. For the projection period (2006-2099) blue, green and red lines represent three emission scenarios (RCP 2.6, RCP 4.5, RCP 8.5), respectively, with the correspondent linear fitting indicated with dashed lines. Shading with grey, light-blue, light-green and pink denotes the 95% confidence intervals of standard deviation for the "good" models in historical runs and projected runs (RCP 2.6, RCP 4.5, RCP 8.5, respectively). The anomalies are relative to 1961-2005.

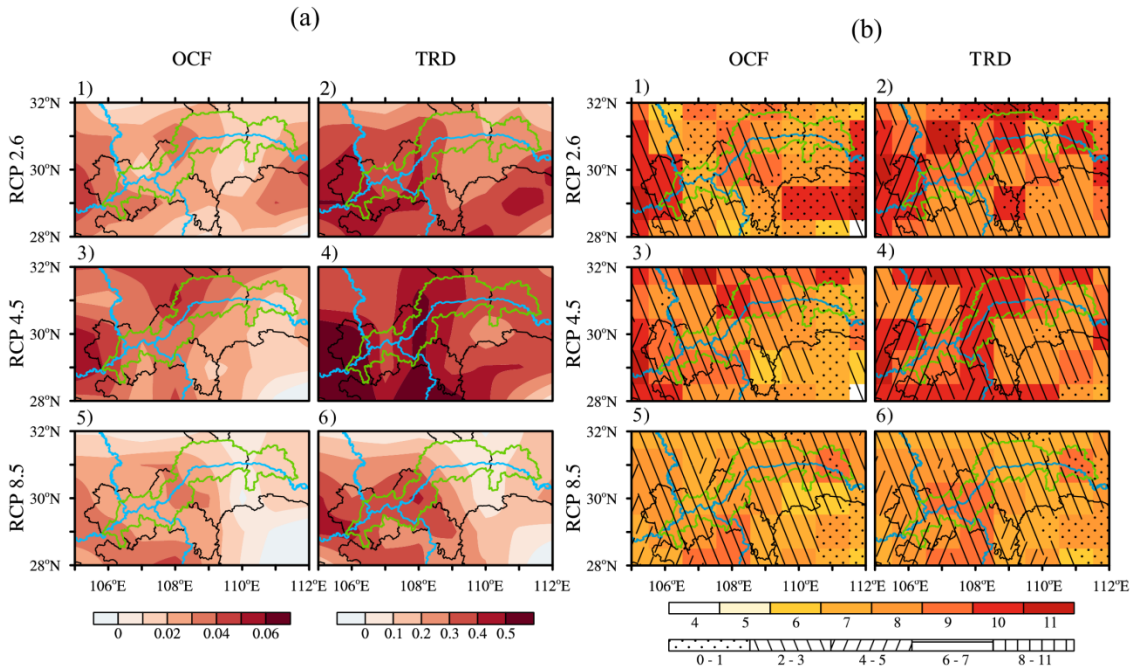

778

779 Figure 5 a) Spatial change trend (per decade) of projected spring occurrence of CREs
780 from 2006 to 2099. b) Number of models among all the 11 models projecting a
781 positive trend of occurrence of CREs (warmer orange corresponding to a positive
782 trend). Left to right correspond to the OCF and TRD describing occurrence of CREs,
783 and upper to lower corresponds to the three emission scenarios from RCP 2.6 to RCP
784 8.5. Colored shading in b) represents the number of models, and dots and hatches
785 shading indicate the number of models with significant trend.

786

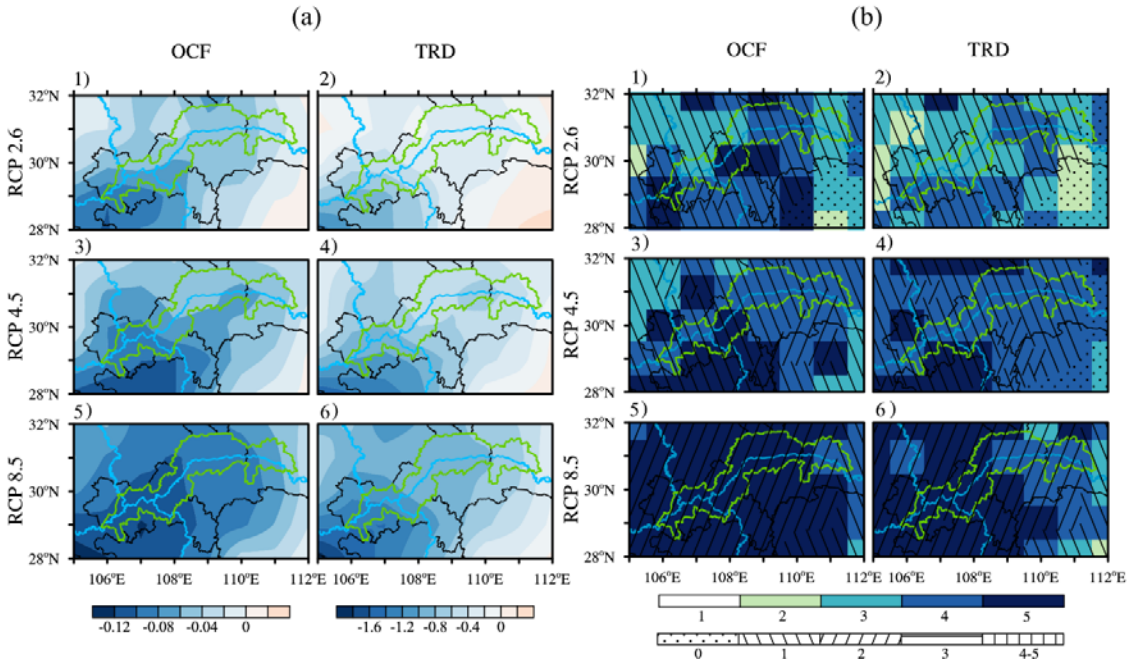

Figure 6 a) As Fig. 5a but for fall, and b) exhibits the number of models among all the 5 models projecting a negative trend of occurrence of fall CREs (cooler blue corresponding to a negative trend).

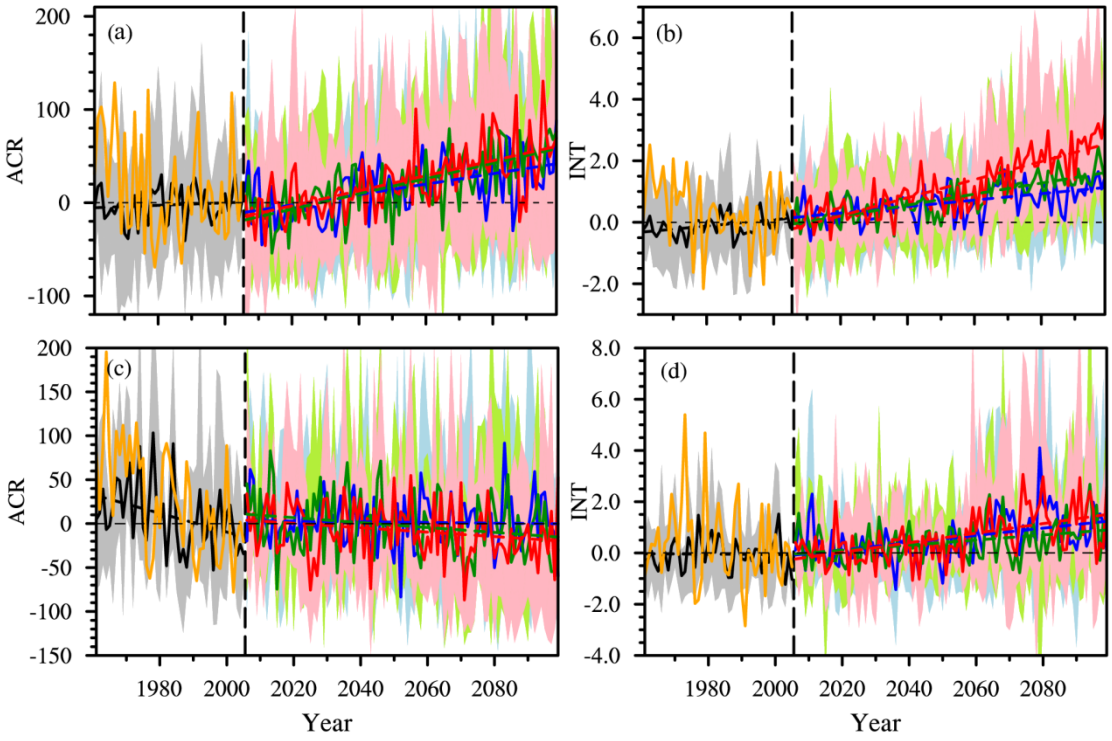

792

793 Figure 7 As Fig. 4 but for ACR and INT.

794

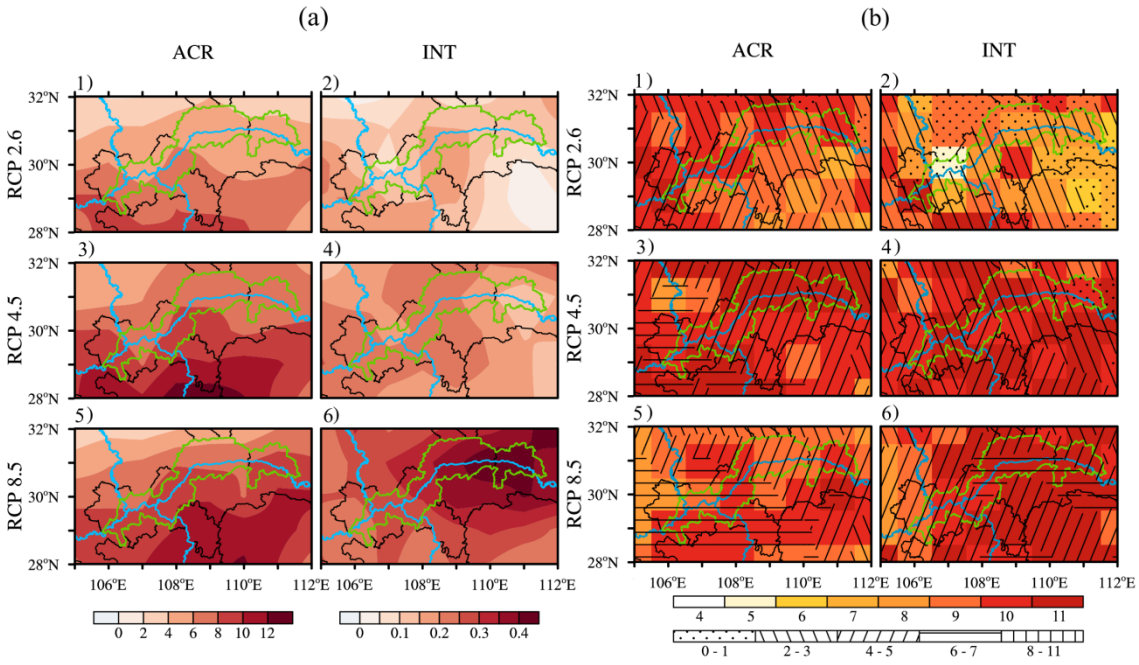

795

796 Figure 8 As Fig. 5 but for ACR and INT describing intensity of spring CREs.

797

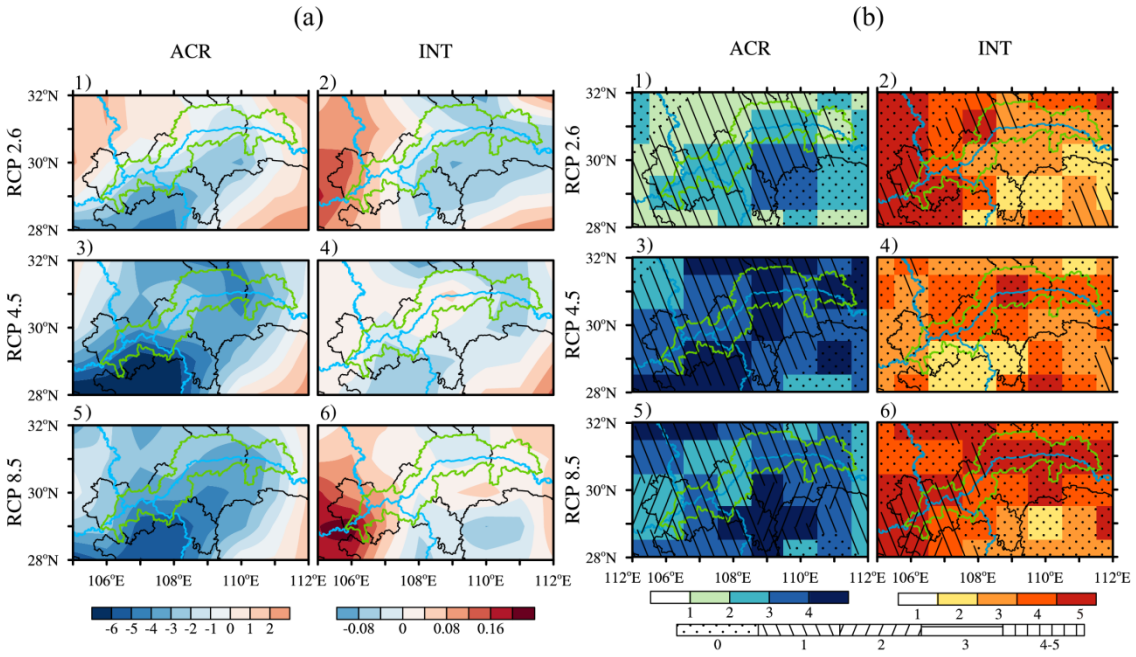

798

799 Figure 9 As Fig.6 but for ACR and INT describing intensity of fall CREs.

800

801

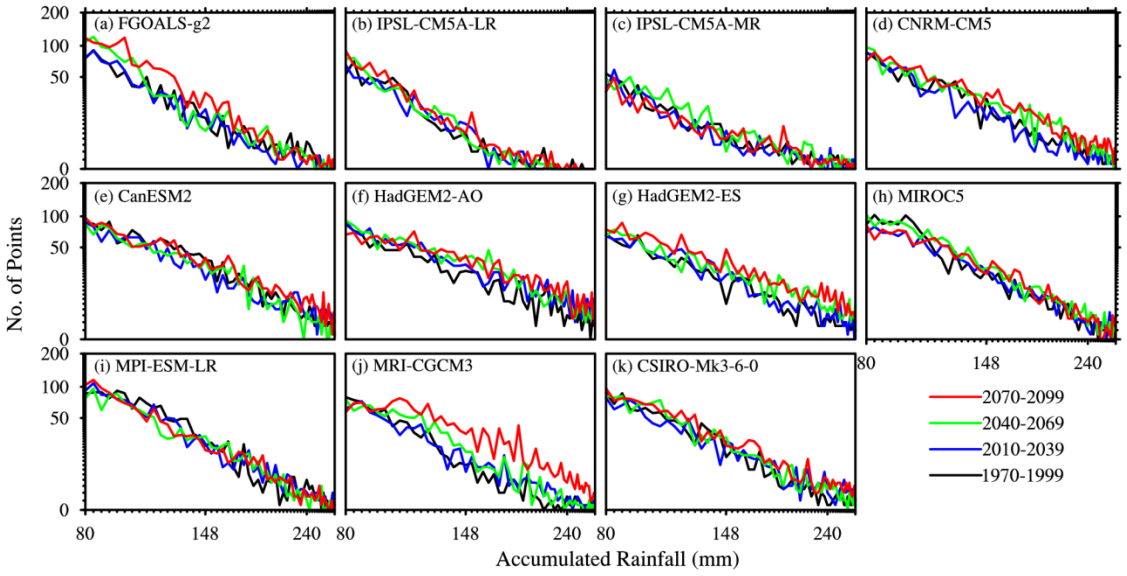

802

803 Figure 10 Frequency distribution of spring ACR in the single CRE for different

804 rainfall bins during different decades of the future derived from “good” CMIP5

805 models under RCP4.5.

806

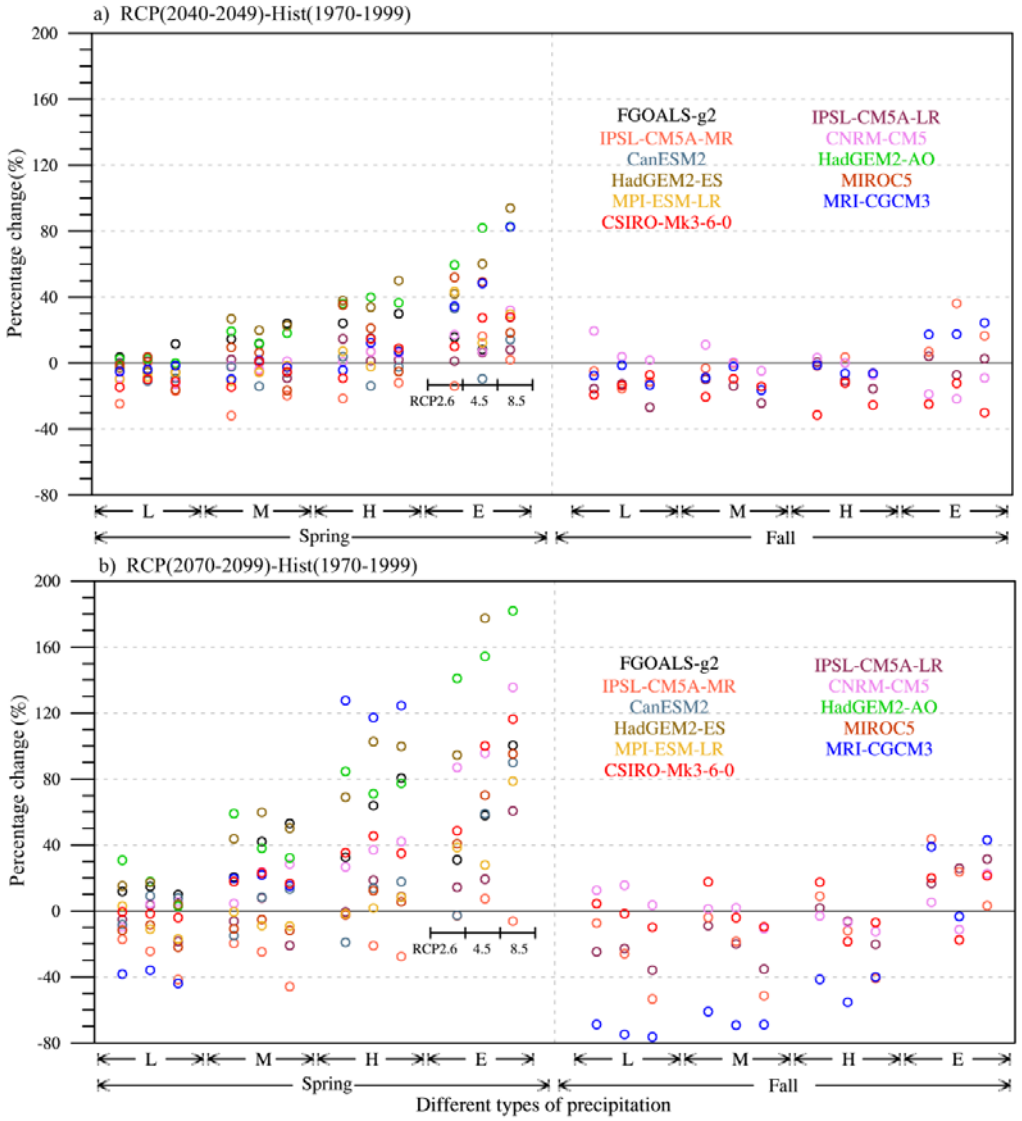

807

808 Figure 11 The change rate of daily rainfall intensity at different categories during

809 CREs. The increments are a) 2070-2099 or b) 2020-2049 relative to the reference

810 period 1970-1999. Response of each “good” CMIP5 models is denoted by different

811 color marks. Different categories of rainfall are shown as L(light rain), M(moderate

812 rain), H(heavy rain), E(exterme rain). Part of models’ mark in b) (the ER growth of

813 MRI-CGCM3 are 422%, 526%, 638% from RCP 2.6 to RCP 8.5 respectively, and the

814 ER growth of HadGEM2-ES is the 235% under RCP 8.5) is not shown due to the

815 oversized change rate.

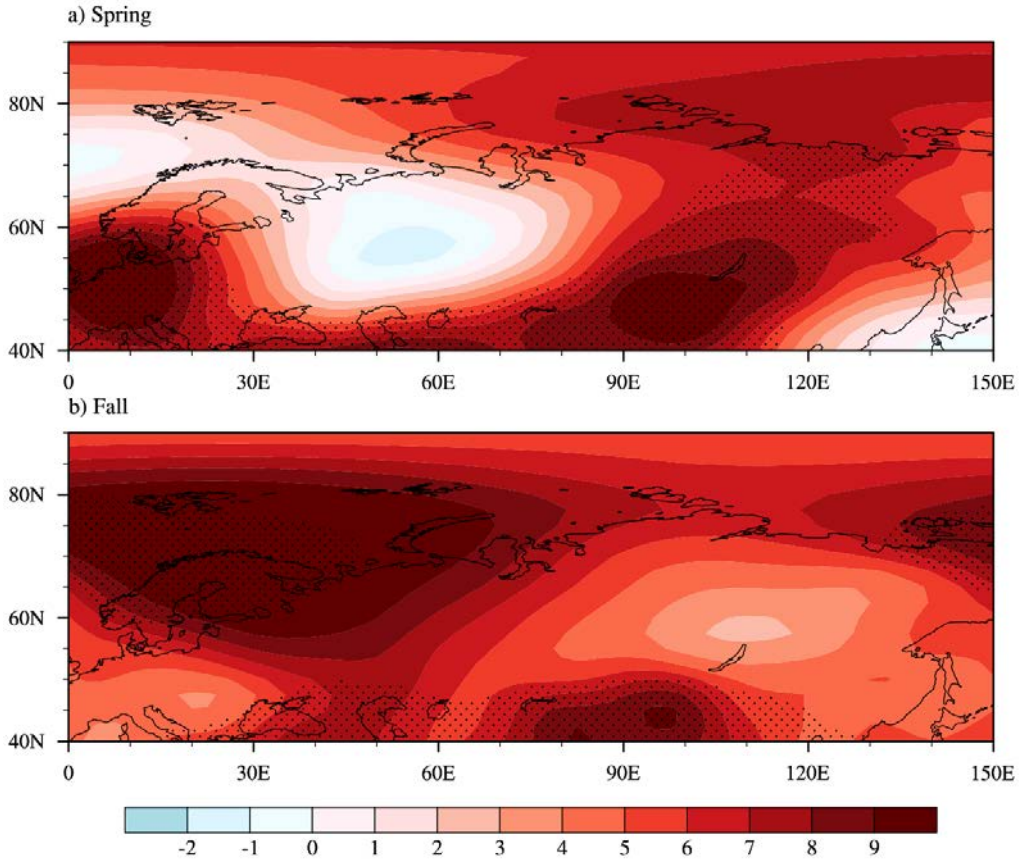

816

817 Figure 12 Change trend of geopotential height at 500hPa level (units: m) in a) spring

818 and b) fall during 1960 - 2018 in the National Center for Environmental Prediction

819 reanalysis I. Regions within shaded in denote the trend or the differences at 99%

820 confidence level.

821

822